metals

MDPI

Article

Creep Deformation Estimation of Single Crystal Ni-Based Superalloy by Optimized Geometrically Necessary Dislocation Density Evaluation

Cristina Motta [1,2,*], Francesco Mastromatteo [2], Niccolò Baldi [2], Elisabetta Gariboldi [1] and Luca Bernardini [2]

[1] Mechanical Engineering Department, Politecnico di Milano, 20156 Milan, Italy; elisabetta.gariboldi@polimi.it
[2] Baker Hughes, 50127 Florence, Italy; francesco.mastromatteo@bakerhughes.com (F.M.); niccolo.baldi2@bakerhughes.com (N.B.)
* Correspondence: cristina.motta@polimi.it or cristina.motta2@bakerhughes.com

Abstract

In the framework of high temperature components, the need to evaluate the accumulated creep damage during service life is fundamental to extend the life of components which are currently deemed as scrap as per design intent. Thus, the life assessment of Ni-based superalloys could be performed in relation to the accumulated creep deformation which represents the limiting factor for serviced components. Despite the different microstructural changes that occur in service life, this work focuses on the possibility to evaluate the material strain by means of electron backscattered diffraction (EBSD). The key point is the identification of the correlation between geometrically necessary dislocation (GND) density derived from EBSD analyses and the reached creep strain for a single crystal Ni-based superalloy. However, the results of GND density are affected by the settings' parameters adopted to perform the analysis by the magnification level and the step size. These two parameters have been optimized by analyzing specimens from interrupted creep tests at strain levels between 0.5% and 10%, in the temperature range between 850 °C and 1000 °C.

Keywords: single crystal Ni-superalloys; creep deformation; GND density; EBSD analysis; life assessment analysis

1. Introduction

Single crystal Ni-based superalloys are performant materials for high temperature applications. In the energy sector, they are exploited for hot gas path components, such as gas turbine blades, for which creep is one of the main damage phenomena [1,2]. The high mechanical performances at high temperatures of these superalloys are related to the microstructure which is constituted by the γ and γ' phases. The γ' phase strengthens the γ matrix by hindering the dislocation motion [3]. The mechanical properties at high temperatures are further enhanced by the absence of any grain boundaries in single crystal materials [4]. When the material is exposed to high temperatures and stresses, during the service life of the component, microstructure evolution and creep deformation occur concurrently and with mutual effects [5]. The microstructural evolution consists of the directional coarsening of the γ' phase, known as the rafting phenomenon, eventual topological inversion of γ and γ' after extensive rafting, widening of γ channel, creep cavitation, precipitation of intermetallic phases, known as topologically closed packed (TCP) phases, formation of microcracks from the existing casting porosity in the interdendritic zones, and increase in dislocation density [6]. These changes in microstructure, which are related to the

Academic Editor: Dariusz Rozumek

Received: 27 November 2025
Revised: 7 January 2026
Accepted: 15 January 2026
Published: 17 January 2026

material chemistry as well as the service conditions [2], result in a progressive loss of the structural properties of the components [7], so that they can be considered as various forms of material microstructural damage. Since these features of damage occur in components during long-term service under conditions leading to concurrent creep deformation [8], once the component reaches its creep serviceability limit according to design intent, it has to be replaced with a new one, with huge impacts on maintenance cost and sustainability [9]. The prediction of the accumulated damage in terms of creep strain or creep life of serviced components could allow not only conventional life assessment analyses in view of extending the service life, but also analyses targeted to check the possible reuse of parts currently classified as scraps and extend their life. Some authors in the literature proposed the use of small punch tests as a potential technique for the assessment of the creep life of serviced components [10,11]. Moreover, other authors used models based on viscoplastic constitutive equations and microstructural parameters for the assessment of the creep life [12]. These models include dislocation density because the creep deformation is dominated by their movement [12,13].

Thus, one fundamental source of microstructural damage is related to the accumulation of dislocations, in particular, in γ matrix channels for the specific case of Ni-based superalloys [14]. The total dislocation density considers both the geometrically necessary dislocations (GNDs) and the statistically stored dislocations (SSDs) [15]. GNDs are characterized by net non-zero burger vectors, leading to crystal misorientation [16]. On the contrary, SSDs do not contribute to the lattice curvature [17]. During plastic deformation, such as that resulting from creep strain, the formation of GNDs in the crystal lattice allows the accommodation of local plastic strain [18] and higher GND levels can be considered related to higher accommodated local plastic strain [19]. Generally, in alloys with a face centered cubic (FCC) crystal, the closed packed planes and directions are, respectively, the {111} and <110> [18]. Thus, dislocations preferentially move in the <110> {111} slip system due to lower energy required for motion [18]. In Ni-based superalloys, at high temperatures the <110> {111} slip system is the main and usually active slip system within the channels of the γ matrix phase [2,20]. As creep strain is accumulated, at the $\{100\}_{\gamma'/\gamma}$ interfaces the dislocation network could evolve toward the end of creep life and depending on service conditions from the <110> diamond shaped dislocation network [2] to the <100> square dislocation network in tertiary creep [20].

Following the above-mentioned effects of creep strain on dislocation densities and their rearrangements, in recent years various authors have analyzed the possibility to adopt parameters derived from scanning electron microscope (SEM) analyses performed on crept samples by electron backscattered diffraction (EBSD) probes and relatively conventional data analyses to identify the parameters suitable for correlation to creep strain, which could be used as a tool in view of the life assessment of components undergoing creep. Focusing on creep as plastic deformation phenomenon, EBSD analyses have been used to assess this type of damage for steels and Ni-based superalloys, both single and poly-crystals [21]. In the literature, different research groups identified different EBSD misorientation parameters to estimate the creep strain. In particular, the parameters considered were the grain reference orientation deviation (GROD) which is defined as the difference between the orientation of a point within a grain and the average orientation of that grain [22], the grain average misorientation (GAM) which represents the average misorientation between one point and its neighbor points in a grain [23], the kernel average misorientation (KAM) which is the misorientation angle between one point and its near neighbors [9], and the geometrically necessary dislocation (GND) density [24]. GNDs are the part of the total dislocation density that could be resolved by EBSD analyses [25]. On the contrary, SSDs could not be detected through EBSD [25]. Rui et al. used the GROD parameter to establish a correlation of this

parameter with the creep strain accumulated by austenitic stainless steels [26]. The same parameter was previously considered in polycrystalline IN738LC alloys by Kobayashi et al., who found an increasing trend between GROD and creep strain [22]. Yoda et al. considered the use of the difference in GAM with the undeformed sample as the suitable parameter to evaluate the creep damage for 316 austenitic stainless steel [23]. Iwasaki et al. used KAM as the correlation parameter for the creep life [9]. KAM was also considered in other studies to evaluate creep damage in Hastelloy X [27] and 10Cr-1Mo-1W-VNbN steel forging [28]. Zhang et al. studied the evolution of creep damage of P91 steel by means of GND density [24]. GND density was finally adopted by Sulzer et al. and Vacchieri et al. to evaluate the creep strain of Ni-based superalloys from high resolution EBSD (HR-EBSD) [14,29]. The use of the EBSD technique permits the acquisition of information related to material strain [30]. EBSD analyses are performed in SEM allowing large area analyses on bulk samples with respect to the transmission electron microscopes (TEM) which could analyze localized areas in thin and more challenging prepared specimens [30]. However, samples for EBSD analyses also require a careful metallographic preparation, which has to be customized for each material [31]. The measurement of GND density is affected by the EBSD setting parameters such as the step size [32].

Focusing on single crystal Ni-based superalloys, only two studies, of Sulzer et al. and Vacchieri et al., approach the evaluation of the creep strain with GND density [14,29]. However, they used HR-EBSD instead of conventional EBSD and they performed analysis with completely different magnification levels and step sizes to each other [14,29]. In particular, Sulzer et al. analyzed very local areas (11.5 × 8.6 μm^2) with a step size of 50 nm, while Vacchieri et al. three hundred times greater areas (170 × 170 μm^2) with a forty times greater step size (2000 nm) [14,29]. It is not possible to derive a standard procedure to perform these types of analyses, which could be potentially extendable to other Ni-based superalloys and material classes. The purpose and novelty of this study is firstly to define a robust and detailed methodology, supported by statistical analyses, to estimate GND density by means of EBSD analyses on specimens from interrupted creep tests, in a range of temperature between 850 °C and 1000 °C, for René N4 superalloy. In particular, the proposed methodology evaluates statistically, in terms of average and standard deviation, firstly the effect of magnification and secondly the effect of step size on GND density. The investigated magnification levels and step sizes in this work are, respectively, 2000× and 500× for the first optimization phase and 800 nm and 500 nm for the second one. The magnification level was selected considering the typical dendritic microstructure of a single crystal Ni- based superalloy, in order to measure GND density in areas including both dendritic and interdendritic regions. After this, the step size was selected to maximize the normalized GND density, independent of the equipment methodology. The evaluation of the effect of previously mentioned factors has been conducted at different levels of temperature and creep strain in order to provide a systematic approach to measure the GND density in René N4 superalloy. In addition to this, a correlation between creep strain and GND density obtained from the optimized methodology has been identified for a set of interrupted creep tests.

2. Materials and Methods

2.1. Materials

The methodological approach to correlate the GND density with creep strain has been designed for René N4, a first-generation single crystal Ni-based superalloys, whose chemical composition is listed in Table 1.

Table 1. Chemical composition of René N4 (wt%).

Element [wt%]	Cr	Co	Al	Ti	W	Mo	Ta	C	B	Nb	Hf	Ni
René N4	9.79	7.39	4.18	3.48	5.91	1.48	4.73	0.06	0.004	0.49	0.13	Bal.

The material has been produced by investment casting in the form of bars and bars of the same batch have been used for the experimental investigation. The longitudinal direction of the bars was the [001] direction of the single crystal. Bars were subjected to René N4 standard heat treatment (HT) cycle, consisting of solution treatment (at temperature between 1240 °C and 1275 °C for 1–4 h) and aging (at temperature between 850 °C and 1100 °C for 8–24 h). For a representative heat treatment of the microstructure refer to reference [33]. After HT, creep specimens with geometry according to ASTM E139-24 [34] were produced. Their diameter was 6.25 mm, and gauge length of 35 mm, with specimen axis along the [001] direction of the crystal.

The creep tests were performed using dead-load machines with calculated engineering stress in the range between 150 MPa and 260 MPa and in the temperature range of 850 °C and 1000 °C, with temperatures T1 < T2 < T3 (T1 = 895 °C, T2 = 925 °C, and T3 = 960 °C). The tensile load was applied along the [001] direction. Creep tests were interrupted at two creep strain levels, below 1% and above 5% (actually, between 5% and 10%). All the levels of investigated creep strain were normalized with respect to the creep strain at rupture. The creep strain at rupture was obtained from one additional creep test that reached the final fracture at intermediate temperature T2. The rupture time for this creep test was in the range between 1200 h and 1500 h. These testing conditions are reported in Table 2.

Table 2. Creep testing condition in terms of temperature and normalized creep strain.

Temperature		Normalized Creep Strain	
RT	Room Temperature	ε_{creep} = 0%	0
T1	895 °C	ε_{creep} < 1% ε_{creep} > 5%	0.06 0.45
T2	925 °C	ε_{creep} < 1% 1% < ε_{creep} < 5% ε_{creep} > 5% ε_{creep} = Rupture	0.04 0.13 0.54 1.0
T3	960 °C	ε_{creep} < 1% ε_{creep} > 5%	0.06 0.54

A reference sample was also considered directly machined from the bar with 0% of creep strain in the [001] direction.

2.2. Sample Preparation and EBSD Analyses

In order to achieve proper specimens to perform EBSD analyses, the creep specimens were first transversally cut in two parts, one of which was then longitudinally cut along the [001] direction, to obtain a section plane corresponding to [001] crystallographic plane. The analyzed area for creep specimens is illustrated in Figure 1.

The sample preparation was performed following the steps illustrated in Table 3. After a quite conventional grinding and polishing, a two-step polishing with colloidal silica was introduced. It is important to highlight that EBSD analysis requires samples to be carefully prepared in order to acquire a high-quality diffraction pattern [31]. The optimization of the previous mentioned process minimized surface deformations induced during sample preparation.

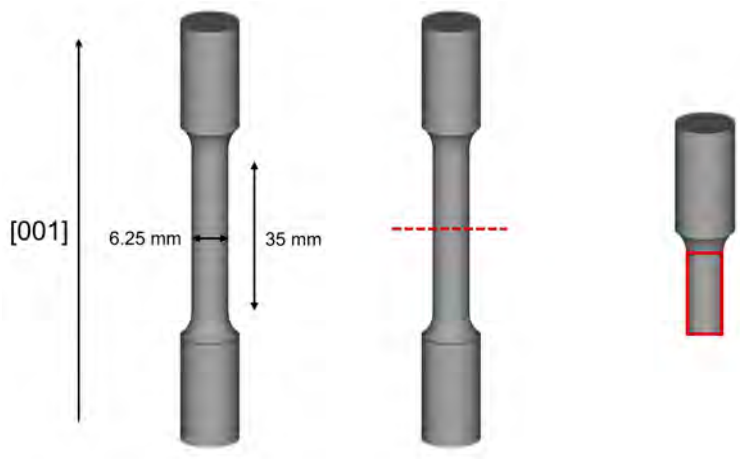

Figure 1. Sample preparation for creep specimens. The analyzed area corresponds to the gauge length along the longitudinal direction which corresponds to the growth direction [001].

Table 3. Procedure of sample preparation for EBSD analysis.

Step	Setting Parameters
Grinding	- 400 grinding paper/30 N/3 min - 600 grinding paper/30 N/3 min - 1200 grinding paper/30 N/3 min
Polishing	- 3 µm diamond paste/20 N/5 min - 1 µm diamond paste/15 N/10 min - 1 µm diamond paste/10 N/5 min
Colloidal silica	- Colloidal silica/10 N/15 min - Colloidal silica/5 N/5 min

After, the microstructure of the reference material was initially examined by means of Field Emission Gun (FEG) SEM Tescan Mira (Tescan, Brno, Czech Republic) on polished and etched sample.

Then, EBSD analyses were performed on the reference and on crept samples, both tilted by 70°, using Focused Ion Beam (FIB) SEM Tescan Amber X (Tescan, Brno, Czech Republic) equipped with Detector symmetry (Oxford Instruments, Abingdon, UK) and the setting parameters used for acquisitions are listed in Table 4.

Table 4. List of the setting parameters used for EBSD analyses.

Setting Parameters for EBSD Analyses	
Accelerating voltage [keV]	20
Beam current [nA]	3
Working distance [mm]	16–20
Exposure time [ms]	24.6

To acquire EBSD maps, AZtec software 5.0 (Oxford Instruments) was used. On each sample, three EBSD analyses were performed at different combinations of magnifications and step sizes in order to define the optimal measurement procedure to estimate the GND density for René N4. The analyzed areas and the step sizes investigated are summarized in Table 5. Three measurements have been repeated in different sample locations to calculate the experimental scatter of results.

Table 5. Setting parameters adopted in various stages of EBSD analyses optimization.

Magnification	Analyzed Area—l × l = Area [μm^2]	Step Size [nm]
2000×	139 × 139 = 19,321	200
500×	556 × 556 = 309,136	800 500

The raw EBSD data were post-processed with AZtec Crystal 2.0 software (Oxford Instruments). A first step of the post-processing procedure consists of the visualization of GND maps to check the presence of occasional residual scratches to define and remove from further analysis steps these areas of relatively high plastic strain induced during sample preparation. This step was fundamental to avoid any alteration in the measurement of GND density. The removed area for each GND map was less than 15%. GND density is estimated considering the misorientation angle approach [35], by the following equation:

$$GND = \frac{\alpha\theta}{bx} \quad (1)$$

where θ is the misorientation angle (KAM), b is the magnitude of the burger vector (0.252 nm), x is the unit length (step size), and α is a constant. This constant, α, could be equal to 2 in the case of pure tilt boundaries or equal to 4 for pure twist boundaries [35]. In this study, α was considered equal to 3. A sensitivity analysis was conducted considering α equal to 2, 3, or 4 and the choice of the α value does not affect the relationship between the creep strain and the GND density. Thus, α equal to 3, for mixed boundaries [36], was adopted. The kernel average misorientation (KAM) analysis was performed using the same software, so that at each analyzed point a misorientation angle θ was calculated.

The presented GND density values have been normalized because each value of the local misorientation, obtained with KAM, is affected by the system of acquisition used, such as the SEM equipment, the EBSD detector, and the software for acquisition [37]. The use of normalized GND density makes clear that the trends rather than actual value of GND density can be adopted on various labs in view of creep strain value assessment.

In particular, data normalization was performed by means of the following equation:

$$\overline{GND} = \frac{GND - GND_{min}}{GND_{Max} - GND_{min}} \quad (2)$$

where $\overline{GND}$ is the normalized GND density, GND is the experimental measured GND density, and GND_{min} and GND_{Max} are, respectively, the minimum (one of the three measurements performed at 500× 800 nm for the reference sample) and the maximum (one of the three measurements performed at 2000× 200 nm for sample tested at T1 and interrupted at $\varepsilon_{creep} > 5\%$) values among all measurements performed in this case study.

3. Results

3.1. Alloy Microstructure

The superalloy under investigation has the typical dendritic microstructure shown in Figure 2. The primary dendrite arm spacing (PDAS) for the analyzed material is about 280 μm. The dendritic cores are characterized by the uniform distribution of the γ′ phase. On the other hand, the interdendritic regions exhibit a not uniform γ′ phase in terms of distribution and size, and the presence of carbides and γ/γ′ eutectics is observed.

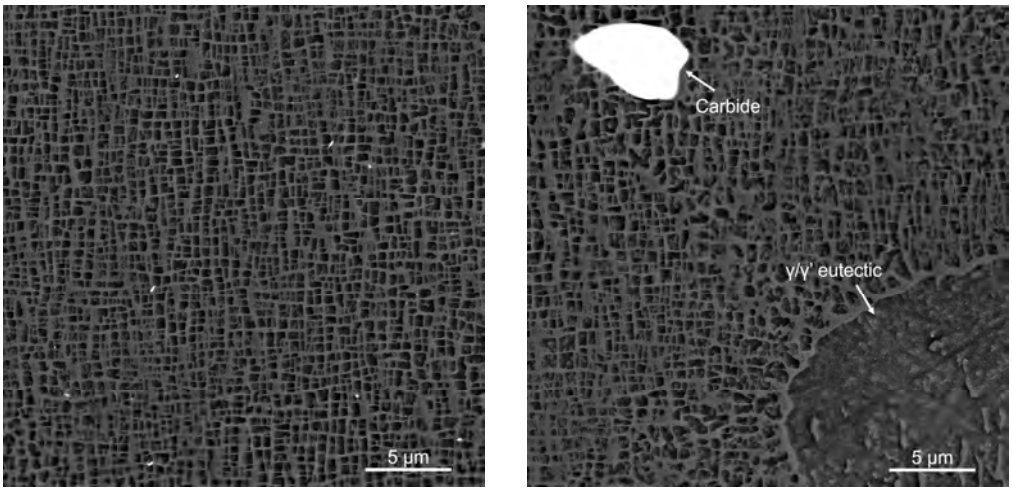

(**a**) (**b**)

Figure 2. Microstructure of the reference material. The dendritic core is shown on the left side (**a**) and interdendritic region on the right one (**b**). The growth direction of the crystal is vertical [001].

3.2. Selection of the Area and Optimization of the Magnification for EBSD Analyses

The first step of the optimization of the EBSD measurement methodology was the definition of the area for EBSD analysis, to select representative sample areas to obtain a significant estimation of the GND of crept specimens. Previous studies carried out on Ni-based superalloys applied various approaches. In particular, Sulzer et al. performed at least three high magnification analyses on each sample, but considering a relatively small area (11.5 × 8.6 µm^2) [14]. On the contrary, Vacchieri et al. analyzed larger areas of (170 × 170 µm^2 [29]) and they acquired more than one area in certain samples. Iwasaki et al. [9] scanned a wide area (about 30 mm^2) at 500×, with a relatively large step size (5 µm).

The present study considered the above-mentioned microstructural features, shown in Figure 2, of René N4 when selecting the area to be analyzed. Due to the lack of uniformity in different regions of the material, low magnification EBSD analyses were performed. In particular, 2000× and 500× were chosen as the magnification levels for comparison. For both magnifications, three areas in different locations were analyzed for each sample. The microstructure in the corresponding areas is shown in Figure 3. In the case of 2000×, the area analyzed is about 2/3 that considered in [29] and, in particular, one dendritic core and fractions of the interdendritic regions were scanned. At the lower magnification, 500×, the scanned area was 16 times larger (see Table 5), and a higher number of dendritic cores and interdendritic regions were analyzed. In Figure 4, an example of the microstructure and its relative IPF map obtained using 500× magnification is shown. For each magnification level investigated, the step size was adjusted to 200 and 800 nm, respectively, for 2000× and 500×, in order to have the same number of analyzed points per scanned area, which also led to the same acquisition and analysis time for both magnification levels. In this step of methodology definition, the magnification effect on GND density measurements was deeply investigated while the step size effect will be studied later.

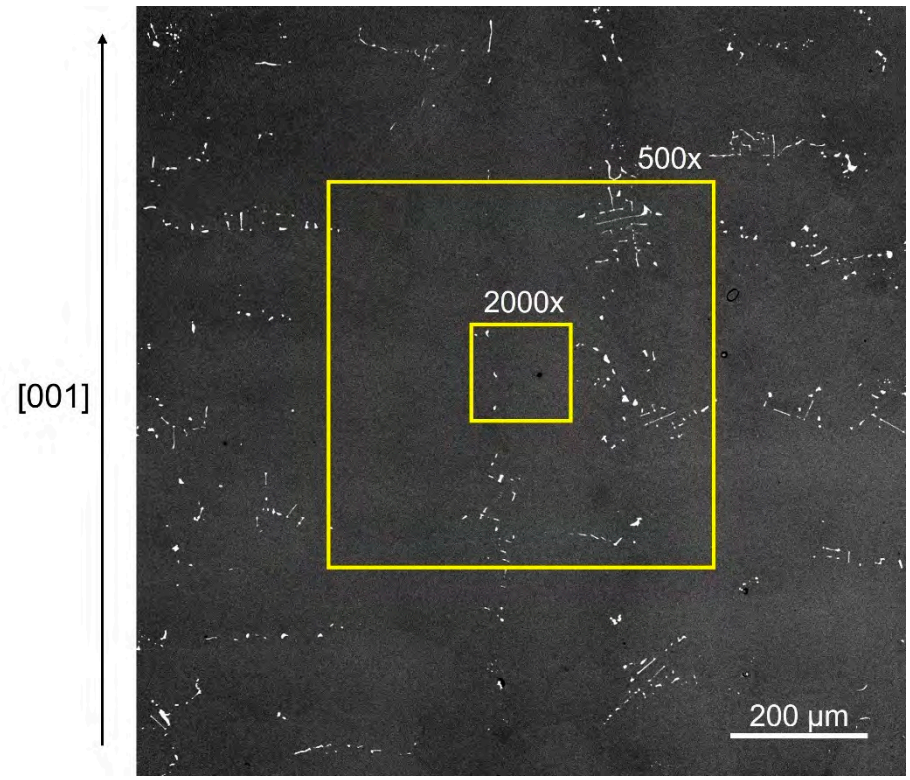

Figure 3. Dendritic structure of reference material at low magnification. Two yellow boxes are related to the analyzed area at the two different magnifications 500× (bigger area) and 2000× (smaller area).

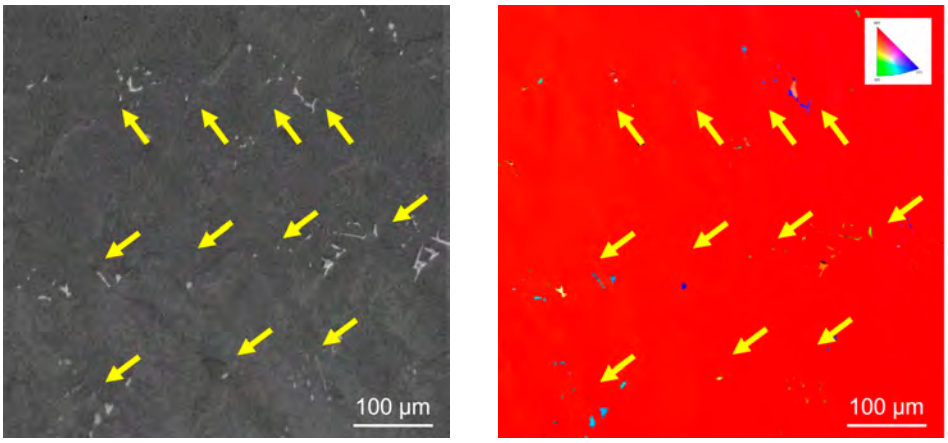

(**a**) (**b**)

Figure 4. Area analyzed SEM image (**a**) and IPF map (**b**) using 500× magnification. The yellow arrows indicate the coarse carbides in interdendritic regions.

To assess the effect of magnification levels on GND density measurements, EBSD analyses were performed on the samples listed in Table 6. The GND maps of the analyzed specimens are shown in Figure 5. By the evaluation of the acquired GND maps and the results shown in Table 6, it was observed that, for a fixed step size, as the magnification increases the GND resolution decreases. Indeed, the $\overline{\text{GND}}$ density average (Avg.) values were lower for EBSD analyses performed at 500× magnification with respect to those at 2000×. Despite this result, the measurement dispersion, evaluated in terms of standard deviation (St.D.), turns out to be generally higher for the 2000× magnification condition (except for the case of T1 with creep strain above 5% sample) with respect to the condition at lower magnification.

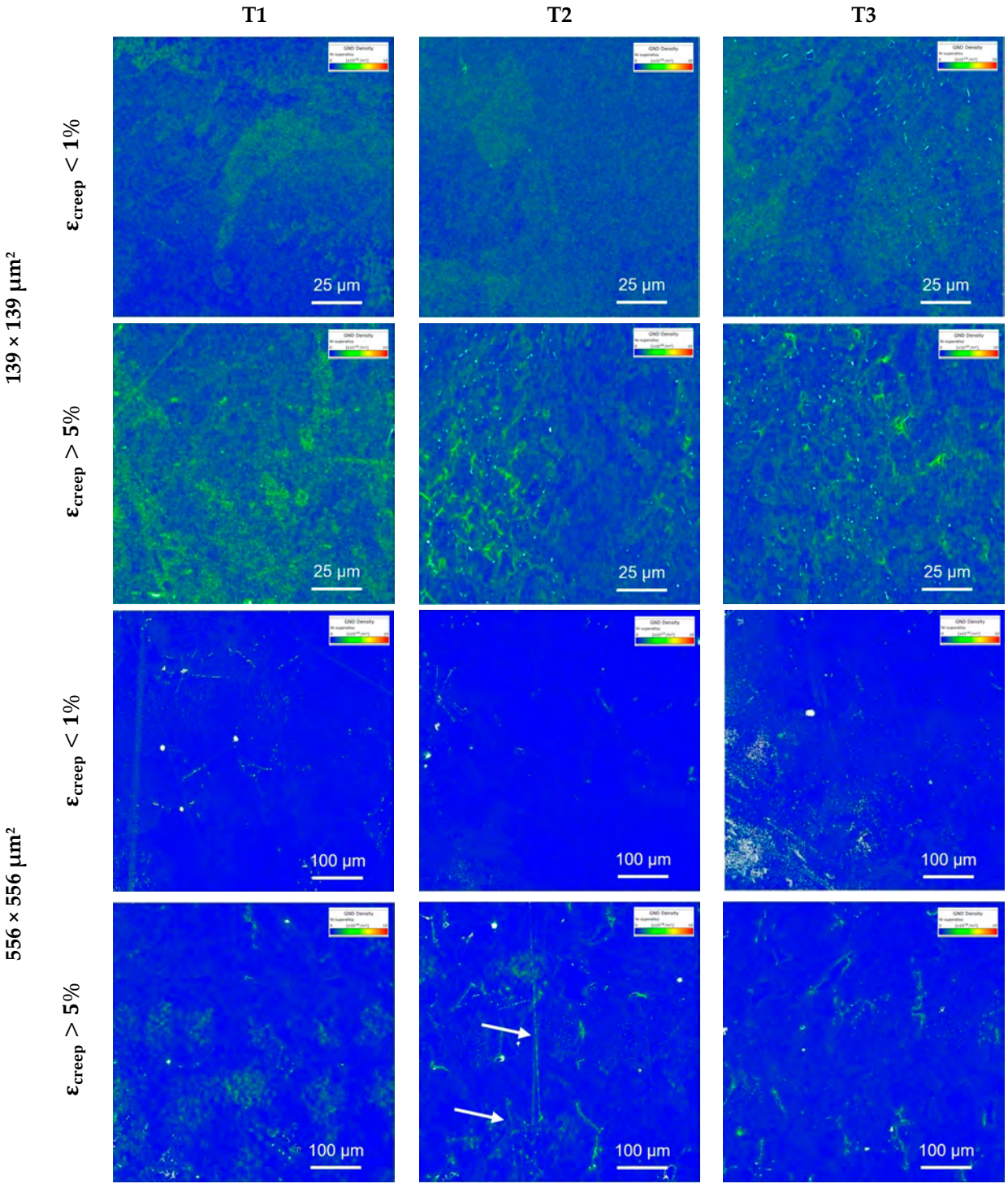

Figure 5. GND density maps on 139 × 139 µm^2 (2000×) and 556 × 556 µm^2 (500×) analyzed area for the three creep conditions (see Table 5). Each condition was analyzed on two different creep strains, below 1% and above 5% of creep strain. Areas related to local deformations added during grinding operations were removed during the post-processing steps, in order not to affect the measurement of GND (for example the areas indicated by white arrows). The tensile load is along the horizontal direction.

Table 6. List of parameters and normalized results of EBSD analyses performed on crept specimens to select the optimal magnification.

Magnification	Analyzed Area [μm²]		Step Size [nm]	Analyzed Points	ε_{creep} [%]	T [°C]	$\overline{GND}$ Density	
	l × l	Area					Avg.	St.D.
2000×	139 × 139	19,321	200	483,025	<1	T1	0.642	0.061
2000×	139 × 139	19,321	200	483,025	>5	T1	0.986	0.024
2000×	139 × 139	19,321	200	483,025	<1	T2	0.784	0.131
2000×	139 × 139	19,321	200	483,025	>5	T2	0.918	0.128
2000×	139 × 139	19,321	200	483,025	<1	T3	0.798	0.053
2000×	139 × 139	19,321	200	483,025	>5	T3	0.713	0.038
500×	556 × 556	309,136	800	483,025	<1	T1	0.057	0.008
500×	556 × 556	309,136	800	483,025	>5	T1	0.281	0.05
500×	556 × 556	309,136	800	483,025	<1	T2	0.068	0.005
500×	556 × 556	309,136	800	483,025	>5	T2	0.213	0.025
500×	556 × 556	309,136	800	483,025	<1	T3	0.104	0.025
500×	556 × 556	309,136	800	483,025	>5	T3	0.194	0.037

In order to perform a detailed analysis of the effect of the magnification level at two ranges of creep strain (<1% and >5%) on GND density measurements, a box plot is created, as shown in Figure 6, and a 2-sample *t*-test is performed. This plot shows that the GND density generally increases as the creep strain increases, regardless of the temperature (except for the condition at 2000× of magnification and at T3). Considering the case of 500×, the differences in $\overline{GND}$ density between the two analyzed strain levels is up to 0.224. Regarding the temperature, no appreciable effect on the $\overline{GND}$ density is observed in Figure 6, while the magnification has a high effect on the $\overline{GND}$ density. The higher magnification increases the $\overline{GND}$ density of one order of magnitude. Thus, the 2-sample *t*-test performed on average and standard deviation of GND measurements, show a calculated *p*-value, respectively, of $p < 0.001$ and $p = 0.02$, revealing a statistical significance for magnification. In detail, it is possible to appreciate that, for the same level of temperature and creep strain configurations, a lower $\overline{GND}$ density average and scatter values for the EBSD analyses performed at magnification of 500×.

On the basis of the above results, and specifically on the higher experimental scatter for GND measurement obtained from EBSD analyses performed at 2000×, EBSD scans at higher magnification were not considered suitable to define a robust methodology to identify a correlation between GND density and creep strain. Thus, the lower magnification (500×) was selected for the further optimization step of this methodology to measure GND density.

3.3. Step Size Optimization: 500 nm vs. 800 nm

Once the best magnification level (500×) was set, an investigation on step size was carried out to refine the GND density measure, keeping constant the scanned area (309,136 μm²). Thus, two different step sizes were chosen, respectively, 500 and 800 nm (this latter was already adopted in the previous optimization step). The number of analyzed areas for each sample was three for both step sizes.

The selection of the step size affects the number of points which are analyzed in the same area. In the specific case here considered, the reduction in the step size up to 500 nm triplicates the number of analyzed points for the area, and also the time for the analysis.

In this step of methodology definition, the EBSD analyses, performed at 500 nm and 800 nm of step size, were carried out on specimens tested at four different conditions of creep strain, including the reference condition at room temperature, as illustrated in Table 7. This table shows that four creep strain ranges were considered rather than the two creep strain ranges used in the previous optimization step. A reference condition at 0% strain and another creep condition with creep strain in the range between 1 and 5% were added. The normalized creep curves of these interrupted tests are plotted in Figure 7 with the addition of the rupture condition.

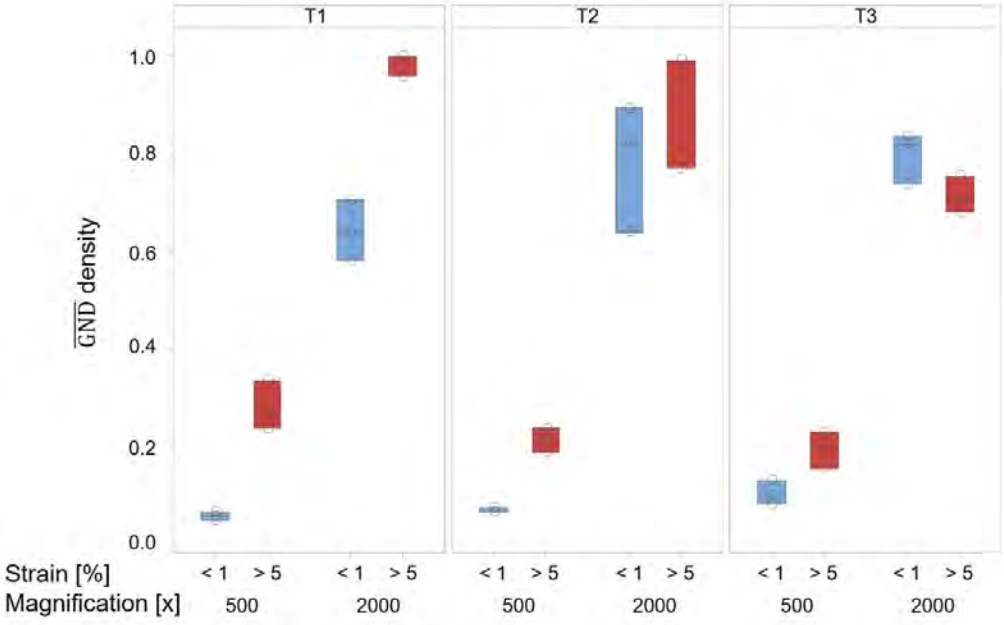

Figure 6. Box plot of overall results of $\overline{GND}$ density for different magnifications, 500× and 2000×. In the box plot, empty circles represent individual values of $\overline{GND}$ density for each acquisition. The light blue colored box identifies samples interrupted at creep strain below 1%, while the red one is related to samples whose accumulated creep strain exceeds 5%. Samples with creep strain between 1 and 5% were not analyzed.

Table 7. List of EBSD analyses performed on creep specimens to optimize the step size with the results in terms of $\overline{GND}$ density. T2 indicates the intermediate temperature, defined in Materials and Methods section, while RT indicates room temperature.

Magnification	Analyzed Area [μm²]		Step Size [nm]	Analyzed Points	ε_{creep} [%]	T [°C]	$\overline{GND}$ Density	
	1 × 1	Area					Avg.	St.D.
500×	556 × 556	309,136	800	483,025	$\varepsilon_{creep} = 0$	RT	0.014	0.013
500×	556 × 556	309,136	800	483,025	$0 < \varepsilon_{creep} \leq 1$	T2	0.068	0.005
500×	556 × 556	309,136	800	483,025	$1 < \varepsilon_{creep} \leq 5$	T2	0.098	0.022
500×	556 × 556	309,136	800	483,025	$5 < \varepsilon_{creep} \leq 10$	T2	0.213	0.025
500×	556 × 556	309,136	500	1,236,556	$\varepsilon_{creep} = 0$	RT	0.117	0.049
500×	556 × 556	309,136	500	1,236,556	$0 < \varepsilon_{creep} \leq 1$	T2	0.205	0.033
500×	556 × 556	309,136	500	1,236,556	$1 < \varepsilon_{creep} \leq 5$	T2	0.270	0.008
500×	556 × 556	309,136	500	1,236,556	$5 < \varepsilon_{creep} \leq 10$	T2	0.311	0.014

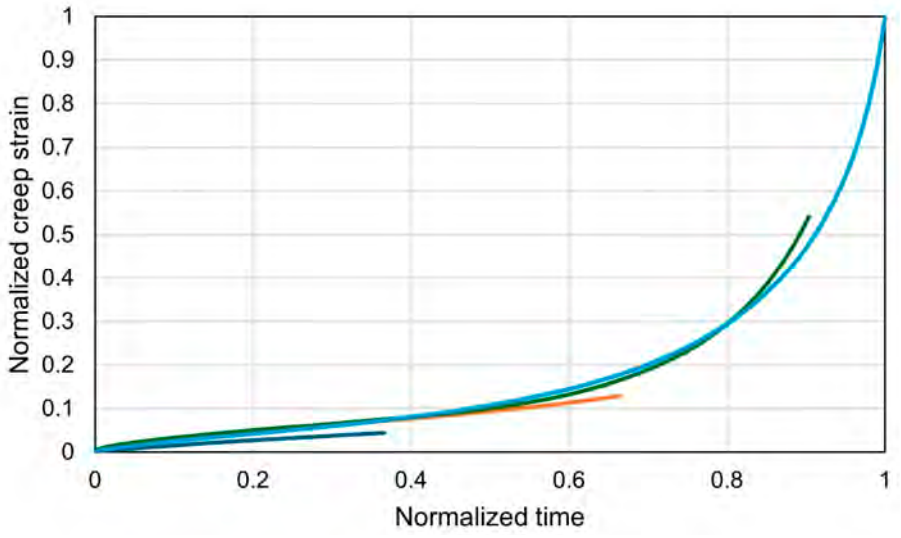

Figure 7. Normalized creep curves of interrupted and rupture creep tests performed at T2. In particular, three tests have been interrupted at normalized creep strain of 0.04 (blue curve), 0.13 (orange curve), 0.54 (green curve), while the light blue curve reached the final fracture.

The normalized GND density measurements, evaluated in terms of average and standard deviation, are reported in Table 7 while the acquired GND density maps are shown in Figure 8.

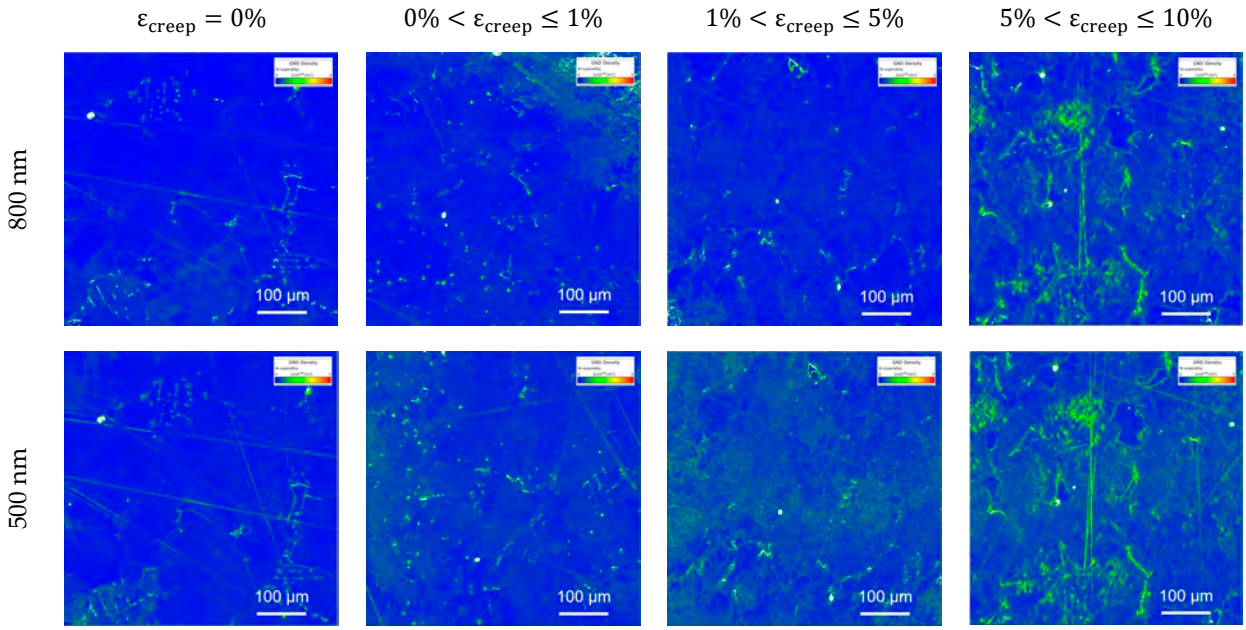

Figure 8. GND density maps comparison for analyses with 800 nm and 500 nm of step size. Areas related to local deformation induced by grinding operations were removed during the post-processing, in order not to affect the measurement of GND. The tensile load is along the horizontal direction.

In order to evaluate the statistical significance of step size, a 2-sample *t*-test is performed on the average and standard deviation of the GND measurements. The calculated *p*-value turns out to be $p < 0.001$ for average, revealing a statistical significance for this parameter. Moreover, Table 7 shows that $\overline{GND}$ values obtained by adopting the smaller step size (500 nm) are higher than those obtained using the higher step size for the EBSD analyses, with similar scatter values. The differences in $\overline{GND}$ density are particularly noticeable below 5% of creep strain, which is most often considered in components.

4. Discussion

By the evaluation of the results related to the assessment of the magnification level to be used, shown in Figure 6, the higher magnification turns out to be less suitable for GND density estimation on crept specimens. In particular, the higher standard deviations of GND density measurements performed at 2000× are up to 26 times greater than those obtained at 500×, under the same range of testing conditions (creep strain < 1% and temperature set to T2). This experimental scatter, observed for higher magnifications, could be most likely due to the effect of the measurement area location. Indeed, the analyzed areas at 2000× of magnification, as shown in Figure 3, include both the dendritic core and the interdendritic regions. Moreover, the relative amount of the interdendritic regions depends on the specific location of the scanned area. Therefore, the higher experimental scatter for 2000× magnification is due to the microstructural heterogeneity of the material. Thus, at this magnification, the quantitative microstructural features are more sensitive to the location of the analyzed area. This holds also for GND density, since it is known that GNDs preferentially accumulate near grain boundaries, sub-boundaries, and carbides [38].

In general, by the evaluation of the results shown in Figure 6, the trend of $\overline{\text{GND}}$ density increases as the creep strain increases, except for the condition at higher temperature, T3, at 2000×. This anomaly for the T3 condition and 2000× is likely due to the heterogeneous microstructure.

The criterion adopted to select the proper magnification to be later used to measure GND density in view of the creep damage assessment was the representativeness of the sample. Thus, the lower magnification (500×), also characterized by a lower experimental data scatter, has been chosen.

Once the magnification has been properly selected, a more detailed study was conducted on specimens considering a single condition of temperature (T2). The purpose of this further investigation is to evaluate the effect of the step size on $\overline{\text{GND}}$ density measurement. In order to perform a deep investigation on step size effect, two additional creep strain conditions were included in this analysis: the reference condition at 0% and an intermediate condition between 1 and 5% of creep strain.

The selection of the optimal step size for EBSD analyses in view of the creep damage assessment should take into account the possibility to discriminate between creep accumulated in different strain ranges. Thus, the $\overline{\text{GND}}$ data density calculated for four strain ranges and listed in Table 7 have been rearranged considering the incremental (average) $\overline{\text{GND}}$ density between a strain range and the following one ($\Delta\overline{\text{GND}}$ density, a dimensionless number as $\overline{\text{GND}}$ density). The three cases, referred to the conditions shown in Table 8, were obtained by the difference in $\overline{\text{GND}}$ between the $\overline{\text{GND}}$ at a higher range of creep strain and $\overline{\text{GND}}$ at the previous lower range of creep strain.

Table 8. Incremental differences in $\overline{\text{GND}}$ density values between consecutive strain conditions.

ΔCreep Strain [%]	**Δ$\overline{\text{GND}}$ Density at 500× 800 nm**	**Δ$\overline{\text{GND}}$ Density at 500× 500 nm**
Condition 1 $(0 < \varepsilon_{\text{creep}} \leq 1) - (\varepsilon_{\text{creep}} = 0)$	0.054	0.088
Condition 2 $(1 < \varepsilon_{\text{creep}} \leq 5) - (0 < \varepsilon_{\text{creep}} \leq 1)$	0.030	0.065
Condition 3 $(5 < \varepsilon_{\text{creep}} \leq 10) - (1 < \varepsilon_{\text{creep}} \leq 5)$	0.115	0.041

It is possible to observe that the lower adopted step size, 500 nm, allows to emphasize the differences in terms of GND density between two consecutive creep strain ranges, for

creep strain conditions lower than 5%. On the other hand, for condition 3, the trend is the opposite. This trend is likely due to the fact that EBSD analyses performed at higher magnification (800 nm) are not able to effectively appreciate smaller creep deformations. In particular, considering the condition 2, the calculated differences for higher and lower step sizes, are, respectively, of 0.030 and 0.065. Hence, the lower step size, characterized by greater GND density difference, significantly enhances the values of $\Delta\overline{GND}$ in this creep strain range, a high-interest range in industrial fields.

By virtue of these results, the best parameters to be used for accurate and robust EBSD analyses to detect GND density turn out to be 500x magnification and 500 nm step size.

Moreover, the plot of the normalized creep strain as a function of the $\overline{GND}$ density results obtained with the optimized procedure for T2 = 925 °C is shown in Figure 9.

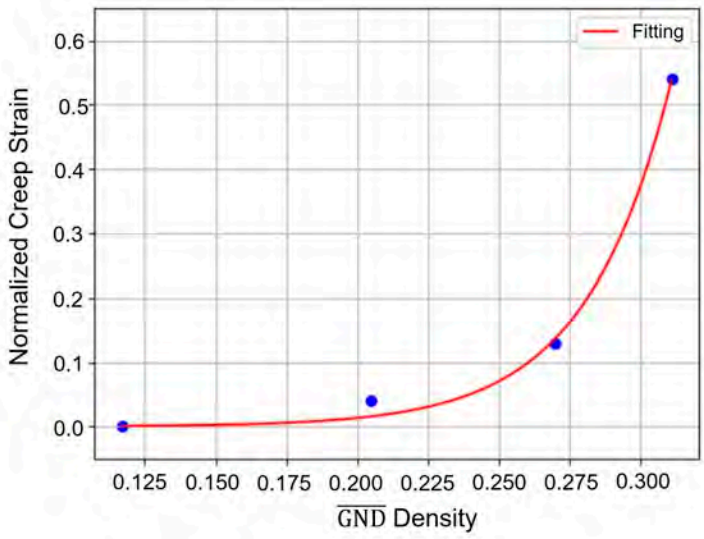

Figure 9. Plot of normalized creep strain as a function of normalized GND density, provided with the best fitting function.

By the evaluation of Figure 9, it is possible to fit accurately the experimental data, R^2 = 0.99, using an exponential function. Moreover, in Figure 9, at a lower creep strain, below 5%, there is a variation in $\overline{GND}$ density equal to 0.153 and this is likely due to a faster accumulation of dislocation density in the first stages of creep life. A similar trend was found by Vacchieri et al. between creep strain and GND density measured through HR-EBSD [29].

The relationship found in Figure 9 shifts leftwards as the temperature increases. This effect could be related to the occurrence of thermally activated phenomena that lead to a faster accumulation of dislocations.

The proposed methodology has been optimized, in terms of magnification and step size, using creep specimens in René N4 material. However, this methodologic procedure, which is able to evaluate the GND density by means of EBSD analyses and post-processes in view of creep strain assessment, is potentially extendable to other Ni-based superalloys. Nevertheless, it should be pointed out that the correlation found between the reached creep strain and the GND density, derived by the application of the optimized methodology on a different cast Ni-based alloy, could be different from the exponential fit obtained for René N4. Indeed, the relationship between creep strain and GND density is affected by other factors, such as the stress level, the test temperature, and the chemical composition and heat treatments performed prior to service, since they affect the initial γ' amount and size, γ/γ' misfit. The role of these factors alters the density of dislocation gliding within channels and at the γ/γ' interface as well as the overall creep life of the material [39,40].

The authors consider it in any case useful to share to the scientific community the methodology followed for EBSD analyses which aimed to provide an accurate and robust GND density measure, to be correlated to creep strain. Moreover, the same principles could be extended to other materials and service conditions in which microstructural inhomogeneities are expected.

5. Conclusions

In this work, a methodology has been proposed to estimate GND density, by means of EBSD analyses, on a Ni-based superalloy in order to detect the accumulated creep strain. In addition to this, following the optimized methodology, a correlation between the creep strain and the GND density has been provided. Once the accumulated creep strain has been measured, the creep life of a component could be derived on strain vs. time curves at the service condition.

The first phase of methodology definition is the identification of the analyzed area that has been experimentally proved to be fundamental to acquire representative GND measurements. In particular, a comparison between normalized GND density measured with different levels of magnification reveals wider experimental scatter for higher magnification analyses. The higher magnification provides standard deviation up to 26 times greater with respect to the lower magnification. This is likely related to the preferential accumulation of dislocations in interdendritic regions, characterized by inhomogeneities presented in the material, such as carbides, eutectics, and not uniform γ' phase. Thus, the lower magnification, in which the scanned area covered several dendrites, was identified as the first optimized parameter to set the EBSD analysis.

The second phase of methodology definition focused on the step size optimization through the evaluation of two levels of this parameter. In this phase, four levels of creep strain at intermediate temperature were studied to achieve a full comprehension of the effect of step size on GND density measurements as a function of creep strain levels. This detailed study suggested the selection of the 500 nm step size. Indeed, for the analyzed Ni-based superalloy, this step size is able to reveal clearly the GND density differences in the creep strain range lower than 5%, which is the range of interest for the detection of creep damage for serviced components.

Moreover, plotting the normalized creep strain as a function of normalized GND density evaluated with the proposed and optimized methodology reveals an exponential trend between these two parameters, likely due to a faster accumulation of dislocations in the first stages of creep life. The $\overline{\mathrm{GND}}$ density increases rapidly, about four times more, for normalized creep strain lower than 0.13, which is lower than 5%.

The advantages of the GND density estimation method are the possibility to obtain a reliable method to estimate the accumulated creep deformation of parts of a given alloy subjected to creep using a quite conventional analysis which is available in a SEM equipped with an EBSD detector and the possibility to find a relationship between them with the creep deformation and to use it for the assessment of creep life. The limitations of this method are related to the dependence on the lab equipment used, the sample preparation, and the alloy considered. The method is particularly suitable for low strain life, and thus for material used for gas turbines. The methodology of EBSD analysis optimization can be easily extended to other Ni-based superalloys, and potentially also to other alloy classes characterized by local microstructural inhomogeneities.

Author Contributions: Conceptualization, C.M. and F.M.; Methodology, C.M., F.M., and L.B.; Formal analysis, C.M.; Investigation, C.M.; Data curation, C.M. and N.B.; Writing—original draft preparation, C.M.; Writing—review and editing, N.B. and E.G.; Supervision, F.M. and E.G. All authors have read and agreed to the published version of the manuscript.

Funding: The APC was funded by Politecnico di Milano.

Data Availability Statement: The original contributions presented in this study are included in the article. Further inquiries can be directed to the corresponding author.

Conflicts of Interest: Authors Cristina Motta, Francesco Mastromatteo, Niccolò Baldi and Luca Bernardini were employed by the company Baker Hughes. The remaining authors declare that the research was conducted in the absence of any commercial or financial relationships that could be construed as a potential conflict of interest.

References

1. Pollock, T.M.; Tin, S. Nickel-Based Superalloys for Advanced Turbine Engines: Chemistry, Microstructure and Properties. *J. Propuls. Power* **2006**, *22*, 361–374. [CrossRef]
2. Gudivada, G.; Pandey, A.K. Recent developments in nickel-based superalloys for gas turbine applications: Review. *J. Alloys Compd.* **2023**, *963*, 171128. [CrossRef]
3. Reed, R.C. *The Superalloys Fundamentals and Applications*, 1st ed.; Cambridge University Press: New York, NY, USA, 2006. [CrossRef]
4. Jo, C.-Y.; Kim, H.-M. Effect of recrystallisation on microstructural evolution and mechanical properties of single crystal nickel based superalloy CMSX-2 Part 2—Creep behaviour of surface recrystallised single crystal. *Mater. Sci. Technol.* **2003**, *19*, 1671–1676. [CrossRef]
5. Xia, W.; Zhao, X.; Yue, L.; Zhang, Z. Microstructural evolution and creep mechanisms in Ni-based single crystal superalloys: A review. *J. Alloys Compd.* **2020**, *819*, 152954. [CrossRef]
6. James, A. Review of rejuvenation process for nickel base superalloys. *Mater. Sci. Technol.* **2001**, *17*, 481–486. [CrossRef]
7. Gu, S.; Gao, H.; Pei, H.; Zhang, C.; Wen, Z.; Li, Z.; Yue, Z. Degradation of microstructural and mechanical properties with serviced turbine blades. *Mater. Charact.* **2021**, *182*, 111582. [CrossRef]
8. Zhao, X.; Zhang, L.; Song, Y.; Niu, X.; Sun, Z.; Zhao, H.; Ni, H.; Yuan, S. Creep deformation and damage characteristics of nickel-based superalloy GH4169. *Mater. Sci. Eng. A* **2023**, *885*, 145589. [CrossRef]
9. Iwasaki, S.; Kobayashi, D.; Tateishi, T.; Yokoyama, R.; Omote, K. Nondestructive Creep Damage Evaluation for Ni-Base Superalloys of Controlled Solidification by Laue Method and Effect of Sample Thickness. In Proceedings of the ASME Turbo Expo 2024: Turbomachinery Technical Conference and Exposition, London, UK, 24–28 June 2024. [CrossRef]
10. Dyson, C.C.; Sun, W.; Hyde, C.J.; Brett, S.J.; Hyde, T.H. Use of small specimen creep data in component life management: A review. *Mater. Sci. Technol.* **2016**, *32*, 1567–1581. [CrossRef]
11. Jeffs, S.; Lancaster, R.J. Small Punch Creep Testing of Single Crystal Superalloys. In Proceedings of the 3rd International Conference on Small Scale Test Techniques, Segau, Liebnitz, Austria, 14–15 November 2014.
12. Gan, W.; Gao, H.; Wen, Z. Based on damage caused by microstructure evolution during long-term thermal exposure to analyze and predict creep behavior of Ni-based single crystal superalloy. *AIP Adv.* **2020**, *10*, 085301. [CrossRef]
13. Zhang, C.; Hu, W.; Wen, Z.; Tong, W.; Zhang, Y.; Yue, Z.; He, P. Creep residual life prediction of a nickel-based single crystal superalloy based on microstructure evolution. *Mater. Sci. Eng. A* **2019**, *56*, 108–118. [CrossRef]
14. Sulzer, S.; Li, Z.; Zaefferer, S.; Haghighat, S.M.H.; Wilkinson, A.; Raabe, D.; Reed, R. On the assessment of creep damage evolution in nickel-based superalloys through correlative HR-EBSD and cECCI studies. *Acta Mater.* **2020**, *185*, 13–27. [CrossRef]
15. Cui, L.; Yu, C.-H.; Jiang, S.; Sun, X.; Peng, R.L.; Lundgren, J.-E.; Moverare, J. A new approach for determining GND and SSD densities based on indentation size effect: An application to additive-manufactured Hastelloy X. *J. Mater. Sci. Technol.* **2022**, *96*, 295–307. [CrossRef]
16. Wright, S.I.; Nowell, M.M.; Field, D.P. A review of strain analysis using Electron Backscatter Diffraction. *Microsc. Microanal.* **2001**, *17*, 316–329. [CrossRef]
17. Wang, R.-Z.; Cheng, L.-Y.; Zhu, S.-P.; Zhao, P.-C.; Miura, H.; Zhang, X.-C.; Tu, S.-T. Semi-quantitative creep-fatigue damage analysis based on diffraction-based misorientation mapping and the correlation to macroscopic damage evolutions. *Int. J. Fatigue* **2021**, *149*, 106227. [CrossRef]
18. Long, A.; Xiong, J.; Wei, B.; Zhang, G.; Feng, G.; Guo, J.; Liu, R. Creep Mechanism and Microstructure Evolution of a Directionally Solidified Ni-Based Superalloy with Different Orientations at 850 °C. *Materials* **2025**, *18*, 1540. [CrossRef] [PubMed]
19. Ma, Y.; Liu, G.; Yang, S.; Chen, R.; Xu, S.; Shen, Y. Effects of Strain Rate on the GND Characteristics of Deformed Polycrystalline Pure Copper. *Metals* **2024**, *14*, 582. [CrossRef]
20. Long, H.; Wei, H.; Liu, Y.; Mao, S.; Zhang, J.; Xiang, S.; Chen, Y.; Gui, W.; Li, Q.; Zhang, Z.; et al. Effect of lattice misfit on the evolution of the dislocation structure in Ni-based single crystal superalloys during thermal exposure. *Acta Mater.* **2016**, *120*, 95–107. [CrossRef]

21. Kobayashi, D.; Miyabe, M.; Kagiya, Y.; Nagumo, Y.; Sugiura, R.; Matsuzaki, T.; Yokobori, A.T. Analysis of damage behaviour based on EBSD method under creep–fatigue conditions for polycrystalline nickel base superalloys. *Mater. Sci. Technol.* **2014**, *30*, 24–31. [CrossRef]
22. Kobayashi, D.; Miyabe, M.; Kagiya, Y.; Sugiura, R.; Yokobori, A.T., Jr. An Assessment and Estimation of the Damage Progression Behavior of IN738LC under Various Applied Stress Conditions Based on EBSD Analysis. *Metall. Mater. Trans. A* **2013**, *44*, 3123–3135. [CrossRef]
23. Yoda, R.; Yokomaku, T.; Tsuji, N. Plastic deformation and creep damage evaluations of type 316 austenitic stainless steels by EBSD. *Mater. Charact.* **2010**, *61*, 913–922. [CrossRef]
24. Zhang, K.; Liu, X.; Fan, P.; Zhu, L.; Wang, K.; Wang, L.; Zhao, C. Characterization of geometrically necessary dislocation evolution during creep of P91 steel using electron backscatter diffraction. *Mater. Charact.* **2023**, *195*, 112501. [CrossRef]
25. Gallet, J.; Perez, M.; Guillou, R.; Ernould, C.; Le Bourlot, C.; Langlois, C.; Beausir, B.; Bouzy, E.; Chaise, T.; Cazottes, S. Experimental measurement of dislocation density in metallic materials: A quantitative comparison between measurements techniques (XRD, R-ECCI, HR-EBSD, TEM). *Mater. Charact.* **2023**, *199*, 112842. [CrossRef]
26. Rui, S.-S.; Shanga, Y.-B.; Fan, Y.-N.; Han, Q.-N.; Niu, L.-S.; Shi, H.-J.; Hashimoto, K.; Komai, N. EBSD analysis of creep deformation induced grain lattice distortion: A new method for creep damage evaluation of austenitic stainless steels. *Mater. Sci. Eng. A* **2018**, *733*, 329–337. [CrossRef]
27. Takaku, R.; Saito, D.; Yoshioka, Y. Effect of Grain Size and Crystal Orientation on Creep Damage Evaluation by Changes of Misorientation in Hastelloy X. *J. Soc. Mater. Sci. Jpn.* **2009**, *58*, 229–234. [CrossRef]
28. Fujiyama, K.; Mori, K.; Kaneko, D.; Kimachi, H.; Saito, T.; Ishii, R.; Hino, T. Creep damage assessment of 10Cr-1Mo-1W-VNbN steel forging through EBSD observation. *Int. J. Press. Vessel. Pip.* **2009**, *86*, 570–577. [CrossRef]
29. Vacchieri, E.; Costa, A.; Parodi, S.; Holdsworth, S.R. Microstructural damage evolution in two Ni based superalloys subjected to different mechanical loading conditions through quantitative EBSD measurements using Cross-Court software. *MATEC Web Conf.* **2014**, *14*, 05001. [CrossRef]
30. Doddapaneni, S.; Kumar, S.; Shama, S.; Shankar, G.; Shettar, M.; Kumar, N.; Aroor, G.; Ahmad, S.M. Advancements in EBSD Techniques: A Comprehensive Review on Characterization of Composites and Metals, Sample Preparation, and Operational Parameters. *J. Compos. Sci.* **2025**, *9*, 132. [CrossRef]
31. Carneiro, Í.; Simões, S. Recent Advances in EBSD Characterization of Metals. *Metals* **2020**, *10*, 1097. [CrossRef]
32. Wright, S.I.; Field, D.P.; Nowell, M.M. Post processing effects on GND calculations from EBSD-based orientation measurements. In Proceedings of the 36th Risø International Symposium on Materials Science, IOP Conference Series: Materials Science and Engineering, Risø, Denmark, 7–11 September 2015; Volume 89. [CrossRef]
33. Miner, R.V.; Gaab, T.P.; Gayda, J. Orientation and Temperature Dependence of Some Mechanical Properties of the Single-Crystal Nickel-Base Superalloy René N4. III-Tension-Compression Anisotropy. In Proceedings of the 114th Annual Meeting of the American Institute of Mining, Metallurgical and Petroleum Engineers, New York, NY, USA, 24–28 February 1985.
34. *ASTM E139-24*; Standard Test Methods for Conducting Creep, Creep-Rupture, and Stress-Rupture Tests of Metallic Materials. ASTM International: West Conshohocken, PA, USA, 2024.
35. Moussa, C.; Bernacki, M.; Besnard, R.; Bozzolo, N. About quantitative EBSD analysis of deformation and recovery substructures in pure Tantalum. In Proceedings of the 36th Risø International Symposium on Materials Science, IOP Conference Series: Materials Science and Engineering, Risø, Denmark, 7–11 September 2015; Volume 89. [CrossRef]
36. Ram, F.; Li, Z.; Zaefferer, S.; Haghighat, S.M.H.; Zhu, Z.; Raabe, D.; Reed, R.C. On the origin of creep dislocations in a Ni-base, single-crystal superalloy: An ECCI, EBSD, and dislocation dynamics-based study. *Acta Mater.* **2016**, *109*, 151–161. [CrossRef]
37. Kamaya, M.; Kubushiro, K.; Sakakibara, Y.; Suzuki, S.; Morita, H.; Yoda, R.; Kobayashi, D.; Yamagiwa, K.; Nishioka, T.; Yamazaki, Y.; et al. Round robin crystal orientation measurement using EBSD for damage assessment. *Mech. Eng. J.* **2016**, *3*, 16-00077. [CrossRef]
38. Birosca, S.; Liu, G.; Ding, R.; Jiang, J.; Simm, T.; Deen, C.; Whittaker, M. The dislocation behaviour and GND development in a nickel based superalloy during creep. *Int. J. Plast.* **2019**, *118*, 252–268. [CrossRef]
39. Carroll, L.J.; Feng, Q.; Pollock, T.M. Interfacial Dislocation Networks and Creep in Directional Coarsened Ru-Containing Nickel-Base Single-Crystal Superalloys. *Metall. Mater. Trans. A* **2008**, *39*, 1290–1307. [CrossRef]
40. Chen, C.; Wang, Q.; Dong, C.; Zhang, Y.; Dong, H. Composition rules of Ni-base single crystal superalloys and its influence on creep properties via a cluster formula approach. *Sci. Rep.* **2020**, *10*, 21621. [CrossRef] [PubMed]